PHYSICAL REVIEW A **87**, 063417 (2013)

Photoelectron diffraction from single oriented molecules: Towards ultrafast structure determination of molecules using x-ray free-electron lasers

Misato Kazama and Takashi Fujikawa
Graduate School of Advanced Integration Science, Chiba University, Yayoi-cho 1-33, Inage, Chiba 263-8522, Japan

Naoki Kishimoto
Department of Chemistry, Graduate School of Science, Tohoku University, Aramaki 6-3, Aoba-ku, Sendai, Miyagi 980-8578, Japan

Tomoya Mizuno, Jun-ichi Adachi, and Akira Yagishita[*]
Photon Factory, Institute of Materials Structure Science, KEK, Oho 1-1, Tsukuba, Ibaraki 305-0801, Japan

(Received 6 March 2013; published 18 June 2013)

We provide a molecular structure determination method, based on multiple-scattering x-ray photoelectron diffraction (XPD) calculations. This method is applied to our XPD data on several molecules having different equilibrium geometries. Then it is confirmed that, by our method, bond lengths and bond angles can be determined with a resolution of less than 0.1 Å and 10°, respectively. Differently from any other scenario of ultrafast structure determination, we measure the two- or three-dimensional XPD of aligned or oriented molecules in the energy range from 100 to 200 eV with a 4π detection velocity map imaging spectrometer. Thanks to the intense and ultrashort pulse properties of x-ray free-electron lasers, our approach exhibits the most probable method for obtaining ultrafast real-time structural information on small to medium-sized molecules consisting of light elements, i.e., a "molecular movie."

DOI: 10.1103/PhysRevA.87.063417 PACS number(s): 33.20.Xx, 61.05.js, 33.80.Eh

I. INTRODUCTION

With the advent of intense short-pulse optical lasers and x-ray free-electron lasers (XFELs), ultrafast molecular imaging has become a major topic in modern physics, chemistry, and biology. Intense short-pulse optical lasers enable us to use recolliding electron wave packets to realize ultrafast molecular imaging. Electrons created by tunneling ionization in molecules in a strong laser field are accelerated and driven back to the molecular core since the electric field in the laser pulse is alternating. In the electron-core recollision, the instantaneous state of the molecules is probed by the electron wave packets (for reviews see [1,2]). On the other hand, XFELs enable us to use the diffraction of ultrashort x-ray pulses or of photoelectrons that are generated within molecules through photoionization by the x-ray pulses. XFELs are expected to permit femtosecond coherent x-ray diffractive imaging at high resolutions of nanometer- to micrometer-sized objects without requiring crystalline periodicity of the samples [3–6]. The reconstructed image is directly obtained from the coherent x-ray diffraction pattern by phase retrieval through the oversampling method [7–11]. Such promising experiments with XFELs have been reported successfully (e.g., [12] and [13]). In addition, photoelectron holography with XFELs has been proposed for ultrafast structure determination of small to medium-sized oriented molecules in the gas phase [14].

In this paper we propose a new scheme to realize a molecular movie with femtosecond time and Ångström spatial resolution for small to medium-sized gas-phase molecules, combining the best of the previously reported theoretical and experimental works. It relies on the availability of XFEL, velocity map imaging of photoelectrons [15], and control of molecular alignment or orientation by strong electric fields of optical lasers [16–21] and is based on the well-developed x-ray photoelectron diffraction (XPD) scenario for surface structure analyses [22–26]. We aim to assess the feasibility of imaging polyatomic molecular structures, i.e., measuring their geometric parameters such as bond lengths and bond angles on a femtosecond time scale using XFEL. The basic physical phenomenon involved is simple and illustrated in Fig. 1. A photoelectron wave is emitted from a core level of a specific atom in an oriented molecule, and then it interferes with a wave elastically scattered by a neighboring atom. Thus, the XPD pattern has the information on the geometric structure around the photoelectron emitter. Such an XPD picture can describe molecular frame photoelectron angular distributions (MFPADs) in a high-energy regime: The intensity of photoelectrons is measured as a function of the detection angle with respect to the molecular z axis, which is usually taken as the highest symmetry axis. In fact, we have successfully reproduced experimental high-energy ($\gtrsim$100 eV) MFPADs of various molecules with our full multiple-scattering XPD calculations [27–29]. MFPAD measurements using the photoelectron–fragment-ion coincidence technique are now widely spread to synchrotron radiation facilities [30–34]. The diffraction pattern for single oriented molecules in a gas-phase sample can then be analyzed to obtain geometric information on the local structure around the photoelectron emitter atom. Measurements of the MFPAD or XPD pattern (hereafter we do not distinguish between MFPAD and XPD) by the coincidence technique require a rapid dissociation accompanied by an axial recoil of fragment ions and also a coincident detection between photoelectrons and fragment ions. In the present scheme for ultrafast molecular imaging, these requirements to get XPD pattern can be circumvented by using the molecular

---

[*] akira.yagishita@kek.jp

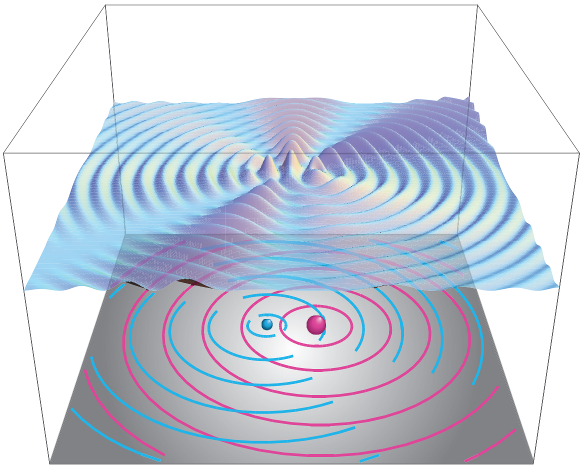

FIG. 1. (Color online) Illustration of x-ray photoelectron diffraction. In a simulation, the interference between a p-type photoelectron wave emitted from the left atom and s-type waves scattered by the right atom makes a fringe pattern. The interference is caused by the phase difference between the two waves due to the path length difference.

alignment or orientation techniques [16–21]. Then, in the present scenario, the XPD of single molecules preoriented by an optical laser in the gas-phase sample can be analyzed at several levels so as to deduce structural information concerning the near-neighbor atoms around the emitter atom.

We show how the molecular structure can be determined from the XPD patterns, based on multiple-scattering XPD calculations. We consider relatively simple molecules, which have different equilibrium geometries; linear CO_2, bent NO_2, planar BF_3, and prolate symmetric top CH_3F molecules. The choice was motivated by considerations to assess the feasibility of molecular imaging for different structures.

The paper is organized as follows. In Sec. II, we introduce the theoretical method to calculate XPD patterns for single oriented molecules. In Sec. III, we describe the methodology of molecular structure determination from the XPD patterns. We apply the methodology to our XPD data for various molecules, which were measured by the photoelectron–fragment-ion coincident technique, to extract information on their ground-state equilibrium geometries in Sec. IV. We show a possible experimental setup for ultrafast photoelectron diffraction imaging in Sec. V. A summary is given in Sec. VI.

II. THEORETICAL DESCRIPTION

Photoemission processes induced by x rays can be described based on many-body scattering theory developed by Hedin *et al.* [35,36] or based on Keldysh Green's function theory developed by Caroli *et al.* [37] and by Fujikawa and Arai [38]. Here we adopt the many-body scattering theory to describe the x-ray-induced photoemission processes. Then we give a general formula for the transition amplitude for the photoemission processes based on multiple-scattering theory, which is the key to our proposal for molecular structure determination. At the end of this section, we show calculated XPD patterns for two cases, to understand their structures that depend on molecular structure.

A. Many-body photoemission theory

An electron-photon interaction $V(t)$ is given in terms of the vector potential $\boldsymbol{A}$ of the x-ray field and a momentum vector $\boldsymbol{p}_i$ of the ith electron as

$$\begin{aligned} V(t) &= \frac{1}{c}\sum_i \boldsymbol{p}_i \cdot \boldsymbol{A}(\boldsymbol{r}_i,t) + \frac{1}{2c^2}\sum_i \{\boldsymbol{A}(\boldsymbol{r}_i,t)\}^2 \\ &= \int dx\, \psi^\dagger(x)\left[\frac{1}{c}\boldsymbol{p}\cdot\boldsymbol{A}(\boldsymbol{r},t) + \frac{1}{2c^2}\boldsymbol{A}(\boldsymbol{r},t)^2\right]\psi(x), \end{aligned} \tag{1}$$

where c is the speed of light, $\boldsymbol{r}_i$ is the position of the ith electron, ψ and $\psi^\dagger$ are field operators, and $x = (\boldsymbol{r},\sigma)$ is a spin coordinate of an electron. The present work is concerned with the one-photon process of photoemission. Hence we take only the linear term of a vector potential, $\boldsymbol{p}\cdot\boldsymbol{A}$, into account. Under this condition, a general expression for the photoelectron current measuring photoelectrons with momentum $\boldsymbol{p}$ is obtained as [39]

$$I(\boldsymbol{p}) = 2\pi \sum_m |\langle \Psi^-_{\boldsymbol{p},m}|H_{ep}|\Psi_0\rangle|^2 \delta(E_0 + \omega - E^*_m - \varepsilon_p), \tag{2}$$

where ω is the photon energy, $\varepsilon_p = \boldsymbol{p}^2/2$ the photoelectron kinetic energy, E_0 the ground-state energy, and E^*_m the mth state energy with a core-hole. The electron-photon interaction Hamiltonian H_{ep} in Eq. (2) is explicitly written as

$$\begin{aligned} H_{ep} &= \int \psi^\dagger(x)\Delta\psi(x)dx, \\ \Delta &\propto \exp(i\boldsymbol{q}\cdot\boldsymbol{r})\boldsymbol{e}\cdot\boldsymbol{p}, \end{aligned} \tag{3}$$

where $\boldsymbol{q}$ is the photon momentum and $\boldsymbol{e}$ is the polarization of it. The many-body photoelectron state $|\Psi^-_{\boldsymbol{p},m}\rangle$ is given in terms of the one-electron photoelectron state $|\phi^-_{\boldsymbol{p}}\rangle$, many-body target state with a core-hole, $|m^*\rangle$, and scattering potential V_m as

$$\begin{aligned} |\Psi^-_{\boldsymbol{p},m}\rangle &= |m^*\rangle|\phi^-_{\boldsymbol{p}}\rangle + \frac{1}{E - H - i\eta}V_m|m^*\rangle|\phi^-_{\boldsymbol{p}}\rangle \\ &= \left(1 + \frac{1}{E - H - i\eta}V_m\right)|m^*\rangle|\phi^-_{\boldsymbol{p}}\rangle, \\ E &= E^*_m + \varepsilon_p, \end{aligned} \tag{4}$$

where H is the total Hamiltonian, which has the form

$$H = H_s + h_m + V_m. \tag{5}$$

The Hamiltonian H_s describes the target including all the electron-electron interactions:

$$H_s = H_v + \varepsilon_c b^\dagger b + V_c b b^\dagger, \tag{6}$$

where H_v is the many-electron Hamiltonian for valence electrons, V_c is the interaction between the core-hole and valence electrons, and ε_c is the energy of the core orbital $|\phi_c\rangle$. The annihilation (creation) operator associated with $|\phi_c\rangle$ is represented by b ($b^\dagger$). The hole state $|m^*\rangle$ satisfies $H^*|m^*\rangle = (H_v + V_c)|m^*\rangle = E^*_m|m^*\rangle$. The ground state $|\Psi_0\rangle = |0_v\rangle|\phi_c\rangle$ is an eigenfunction of $H_v + \varepsilon_c$. The inelastic scattering potential V_m in Eqs. (4) and (5) is given in terms of the electron-target interaction V_{es},

$$V_m = V_{es} - \langle m^*|V_{es}|m^*\rangle. \tag{7}$$

The one-particle photoelectron state $|\phi_{\boldsymbol{p}}^{-}\rangle$ satisfies the following equation for the Hermitian one-electron Hamiltonian h_m,

$$\begin{aligned} h_m|\phi_{\boldsymbol{p}}^{-}\rangle &= \varepsilon_p|\phi_{\boldsymbol{p}}^{-}\rangle, \\ h_m &= T_e + \langle m^*|V_{es}|m^*\rangle, \end{aligned} \tag{8}$$

where T_e is the kinetic energy operator. Thus Eq. (2) is rewritten as

$$\begin{aligned} I(\boldsymbol{p}) &= 2\pi\sum_m |T(\boldsymbol{p}m^*,0)|^2\delta(E_0+\omega-E_m^*-\varepsilon_p), \\ T(\boldsymbol{p}m^*,0) &= \langle\phi_{\boldsymbol{p}}^{-}|\langle m^*|(1+V_mG)H_{ep}|\Psi_0\rangle, \\ G &= \frac{1}{E-H+i\eta}. \end{aligned} \tag{9}$$

In the next step, we introduce the projection operators $P=|m^*\rangle\langle m^*|$ and $Q=1-P$ to obtain a practical formula to calculate the transition amplitude $T(\boldsymbol{p}m^*,0)$. In this context, we rewrite H as

$$\begin{aligned} H &= \tilde{H}+\tilde{V}, \\ \tilde{H} &= H_s + h_m + QV_mQ, \\ \tilde{V} &= PV_mQ + QV_mP. \end{aligned} \tag{10}$$

The Green's function corresponding to the "unperturbed" Hamiltonian $\tilde{H}$ is defined as

$$\tilde{G}(E) = \frac{1}{E-\tilde{H}+i\eta}. \tag{11}$$

Then the transition amplitude is written as [40]

$$\begin{aligned} T(\boldsymbol{p}m^*,0) &= i\eta\langle\phi_{\boldsymbol{p}}^{-}|\frac{1}{\varepsilon_p - h_m - \Sigma_m + i\eta} \\ &\quad\times\langle m^*|(1+\tilde{V}\tilde{G})H_{ep}|\Psi_0\rangle, \end{aligned} \tag{12}$$

where Σ_m is the optical potential and is defined as

$$\Sigma_m(E) = \langle m^*|\tilde{V}\tilde{G}(E)\tilde{V}|m^*\rangle. \tag{13}$$

The optical potential is an energy-dependent non-Hermitian potential and describes the damping of a photoelectron inside the target. Here we define the new one-electron function $|\psi_{\boldsymbol{p}}^{-}\rangle$ as

$$|\psi_{\boldsymbol{p}}^{-}\rangle \equiv \frac{-i\eta}{\varepsilon_p - h_m - \Sigma_m^{-}(E) - i\eta}|\phi_{\boldsymbol{p}}^{-}\rangle, \tag{14}$$

which satisfies the equation

$$[h_m + \Sigma_m^{-}(E)]|\psi_{\boldsymbol{p}}^{-}\rangle = \varepsilon_p|\psi_{\boldsymbol{p}}^{-}\rangle. \tag{15}$$

The damping one-electron function $|\psi_{\boldsymbol{p}}^{-}\rangle$ describes a photoelectron state scattered not only by the static potential $\langle m^*|V_{es}|m^*\rangle$ but also by the energy-dependent optical potential $\Sigma_m^{-}(E)$: $|\psi_{\boldsymbol{p}}^{-}\rangle$ damps inside the target due to the non-Hermitian optical potential. Since we consider the excitation from the core $|\phi_c\rangle$ in the present discussion, the electron-photon interaction Hamiltonian H_{ep} can be approximated as

$$H_{ep} \approx \sum_{\boldsymbol{p}}\langle\boldsymbol{p}|\Delta|\phi_c\rangle c_{\boldsymbol{p}}^{\dagger}b, \tag{16}$$

where $c_{\boldsymbol{p}}^{\dagger}$ is the creation operator of a photoelectron with energy ε_p. When the photoelectron kinetic energy ε_p is higher than the virtual excitation energy of the target (typically about 10 eV), we can use the approximate closure relation of $\sum_{\boldsymbol{p}}|\boldsymbol{p}\rangle\langle\boldsymbol{p}| \approx 1$. Finally, we obtain

$$\begin{aligned} T(\boldsymbol{p}m^*,0) &\approx \langle\psi_{\boldsymbol{p}}^{-}|\langle m^*|(1+\tilde{V}\tilde{G})|0_v\rangle\Delta|\phi_c\rangle \\ &= \langle\psi_{\boldsymbol{p}}^{-}|\Delta|\phi_c\rangle S_m + \sum_{n\neq m}\langle\psi_{\boldsymbol{p}}^{-}|\langle m^*|\tilde{V}\tilde{G}|n^*\rangle\Delta|\phi_c\rangle S_n. \end{aligned} \tag{17}$$

The intrinsic amplitude S_m describes the reduction due to the core-hole production,

$$S_m = \langle m^*|0_v\rangle = \langle m^*|b|\Psi_0\rangle. \tag{18}$$

For the main peak of the core excitation spectra ($m^*=0^*$), Eq. (17) can be further simplified because the second term should be about two digits smaller than the first one:

$$T(\boldsymbol{p}0^*,0) = \langle\psi_{\boldsymbol{p}}^{-}|\Delta|\phi_c\rangle S_0. \tag{19}$$

The intrinsic amplitude S_0 can be approximated as 1. Note that the second term in Eq. (17) is comparable to the first one in the case of loss peaks [35].

B. Multiple-scattering x-ray photoelectron diffraction theory

To calculate the transition amplitude $\langle\psi_{\boldsymbol{p}}^{-}|\Delta|\phi_c\rangle$ with elastic scatterings from constituent atoms of a molecule, we employ a site t-matrix expansion of the photoelectron wave function $|\psi_{\boldsymbol{p}}^{-}\rangle$ [41,42]:

$$\begin{aligned} \langle\psi_{\boldsymbol{p}}^{-}|\Delta|\phi_c\rangle &= \langle\phi_{A\boldsymbol{p}}^{-}|\Delta|\phi_c\rangle + \sum_{\alpha(\neq A)}\langle\phi_{\boldsymbol{p}}'|t_\alpha g_A\Delta|\phi_c\rangle \\ &\quad + \sum_{\beta\neq\alpha(\neq A)}\langle\phi_{\boldsymbol{p}}'|t_\beta g_0 t_\alpha g_A\Delta|\phi_c\rangle + \cdots, \end{aligned} \tag{20}$$

where $\langle\phi_{\boldsymbol{p}}'|$ is the decaying plane-wave function under the influence of the imaginary part of the optical potential, and $\langle\phi_{A\boldsymbol{p}}^{-}|$ is the photoelectron wave function influenced only by the potential of the photoelectron emitter A. The Green's function g_A is influenced only by the potential of the emitter A: $g_A = g_0 + g_0 t_A g_0$. t_α is the site t matrix at site α, which describes full-multiple scattering inside the potential of α. Each term in Eq. (20) has a clear physical meaning: The first term describes the direct photoemission amplitude Z_1 without scatterings from surrounding atoms; the second term, the single scattering amplitude Z_2; and the third term the double scattering amplitude Z_3. Here we assume x-ray propagation to the positive x direction with the polarization parallel to the z axis. In this case, the electron-photon interaction operator is given by

$$\Delta \propto \exp(iqx)p_z. \tag{21}$$

For multipolar expansion of the photon field, power series expansion is widely used [43]:

$$\begin{aligned} \exp(iqx)p_z &= p_z + iqxp_z - \frac{q^2x^2}{2}p_z + \cdots \\ &= p_z + \frac{iq}{2}(xp_z + zp_x) + \frac{iq}{2}(xp_z - zp_x) \\ &\quad - \frac{q^2}{2}(r^2 - y^2 - z^2)p_z + \cdots. \end{aligned} \tag{22}$$

In the second line of Eq. (22), the first term describes the electric dipole (E1) operator, the second electric quadrupole (E2), and the third magnetic dipole (M1). In the fourth term, the electric dipole term of $r^2 p_z$ again appears: The E1 operator in the power series expansion usually does not contain this term, because it is negligible when the photon energy is not so high. In the soft x-ray regime (<1 keV), the condition $qr_c \ll 1$ is satisfied, where r_c is the size of the core orbital $|\phi_c\rangle$. Then $\exp(iqx)p_z$ can be approximated by the first term in Eq. (22). However, in the hard x-ray regime (greater than several keV), we need to consider the higher terms of the multipolar expansion as well. It should be noted that nondipole effects become prominent in high-energy photoemission [44]. Here we focus on photoemission in the soft x-ray regime, where the condition $qr_c \ll 1$ is satisfied, so that we take only the first term in Eq. (22) in the following discussion. Then Δ is written in the dipole length form as

$$\begin{aligned} \Delta &= r \sum_{m=-1}^{1} c_m Y_{1m}(\hat{\boldsymbol r}), \\ c_0 &= \sqrt{\frac{4\pi}{3}} e_z, \quad c_{\pm 1} = \sqrt{\frac{2\pi}{3}} (\mp e_x + i e_y). \end{aligned} \tag{23}$$

By applying multiple-scattering renormalization to Eq. (20), finally we obtain the full multiple-scattering formula [29,42]:

$$\begin{aligned} \langle \psi_{\boldsymbol p}^- | \Delta | \phi_c \rangle &= \sum_\alpha e^{-i\boldsymbol p \cdot \boldsymbol R_{\alpha A}} \sum_{LL'} Y_{L'}(\hat{\boldsymbol p}) [(1-X)^{-1}]^{\alpha A}_{L'L} M_{LL_c}, \\ (1-X)^{-1} &= 1 + X + X^2 + \cdots, \\ X^{\alpha\beta}_{LL'} &= (1-\delta^{\alpha\beta}) t^\alpha_l(p) G_{LL'}(p\boldsymbol R_{\alpha\beta}), \end{aligned} \tag{24}$$

where $\boldsymbol R_{\alpha A}$ is the position vector of the scatterer α measured from the photoelectron emitter A, and M_{LL_c} is the dipole excitation matrix element [L is an abbreviation of indices (l,m)]. $G_{L'L}(p\boldsymbol R_{\alpha A})$ describes electron propagation from site A with angular momentum L to site α with L': It reflects the geometric structure of a molecule. The analytical form of $G_{L'L}(p\boldsymbol R_{\alpha A})$ is written as

$$\begin{aligned} G_{L'L}(p\boldsymbol R_{\alpha A}) = &-\frac{4\pi}{R_{\alpha A}} e^{ipR_{\alpha A}} C_l(pR_{\alpha A}) C_{l'}(pR_{\alpha A}) \\ &\times Y_L(\hat{\boldsymbol R}_{\alpha A}) Y^*_{L'}(\hat{\boldsymbol R}_{\alpha A}). \end{aligned} \tag{25}$$

The spherical correction $C_l(z)$ is defined by the spherical Hankel function as

$$h_l(z) = \frac{i^{-l-1}\exp(iz)}{z} C_l(z). \tag{26}$$

C. Prototypical examples of practical calculations

In practical calculations we employ the muffin-tin approximation for molecular potentials. A scattering potential inside a muffin-tin sphere is calculated by the nonlocal optical atomic potential [45], which enables us to take many-body effects into account. The inclusion of many-body effects is crucial for proper evaluation of elastic scattering from constituent atoms. The detailed procedure of phase shift calculation is reported in Ref. [29].

1. XPD pattern of CO

Figure 2 shows calculated C 1s XPD patterns of CO with its z axis parallel to the light polarization $\boldsymbol e$ at $\varepsilon_p = 150$ eV. The bond length of the molecule was fixed at the equilibrium distance in the ground state, 1.128 Å. A two-dimensional (2D) XPD image, which is the projection of a 3D XPD on the x-z plane, obtained by the full multiple-scattering calculation is shown in Fig. 2(a), and a polar plot of it is given in Fig. 2(b). The polar plot has small lobes at $\theta \sim \pm 60^\circ$ and $\pm 120^\circ$, where θ is measured from the z axis. To clarify the origin of the lobes, we have performed calculations by controlling the order of scattering purposefully. The results of such computational experiments are shown in Fig. 2(c). The XPD pattern with double scattering is almost identical to that with full multiple scattering. It is interesting that the XPD pattern with single scattering in Fig. 2(c) has the characteristic lobes seen in that with full multiple scattering. This means that the origin of the small lobes at $\theta \sim \pm 60^\circ$ and $\pm 120^\circ$ are essentially attributed to the interference between the direct wave from the C atom and the single-scattering wave from the O atom. Further, we examine in detail the single-scattering XPD structure by the graphical representations of $|Z_1|^2$, $|Z_2|^2$, and $2\mathrm{Re}(Z_1^* Z_2)$ in Fig. 2(d), where $|Z_1 + Z_2|^2 = |Z_1|^2 + |Z_2|^2 + 2\mathrm{Re}(Z_1^* Z_2)$. The profile of $|Z_1|^2$ shows a $\cos^2\theta$ distribution due to the dipole transition $s \to p$ without any scattering. The absolute square of the single-scattering amplitude, $|Z_2|^2$, shows a strong intensity toward the O atom (i.e., the forward direction). The interference between Z_1 and Z_2, $2\mathrm{Re}(Z_1^* Z_2)$, exhibits large negative values around $\theta \sim \pm 30^\circ$ and small positive values around $\theta \sim \pm 60^\circ$, which cause the lobe shapes at $\theta \sim \pm 60^\circ$. Similarly the destructive interference around $\theta \sim \pm 150^\circ$ and the constructive interference around $\theta \sim \pm 120^\circ$ cause the small lobes at $\theta \sim \pm 120^\circ$. The profile of $|Z_1|^2$ does not depend on the molecular structure, because it does not include elastic scatterings. If we change the bond length in the calculations, the peak intensity of $|Z_2|^2$ along the molecular axis is changed, although the peak direction along the axis is held. In contrast, the profile of the interference between them, $2\mathrm{Re}(Z_1^* Z_2)$, drastically changes: Its peak and dip positions and their intensities vary with the bond length. Thus, when we use XPD patterns as probes of the molecular structure, we should select the preferable conditions (e.g., the angle between the light polarization vector and the molecular z axis, or the photoelectron kinetic energy) to clearly observe the interference effects in the patterns.

Note that for molecules consisting of more than several atoms, scatterings of higher order must be included to get the same XPD profile as the full multiple-scattering one. The necessary order of scattering to get convergence is dependent on the photoelectron kinetic energy as well: The lower the kinetic energy is, the higher the order of terms of scattering that must be included. Even in the high-energy region we should consider at least N_a-times scatterings in our experience, where N_a is the number of atoms in the relevant molecule. When we treat large enough systems, the calculated XPD patterns with a finite number of scatterings do not converge to that with full multiple scattering. In this case, the full multiple scattering must be considered using the multiple-scattering renormalization [$(1-X)^{-1}$ in Eq. (24)].

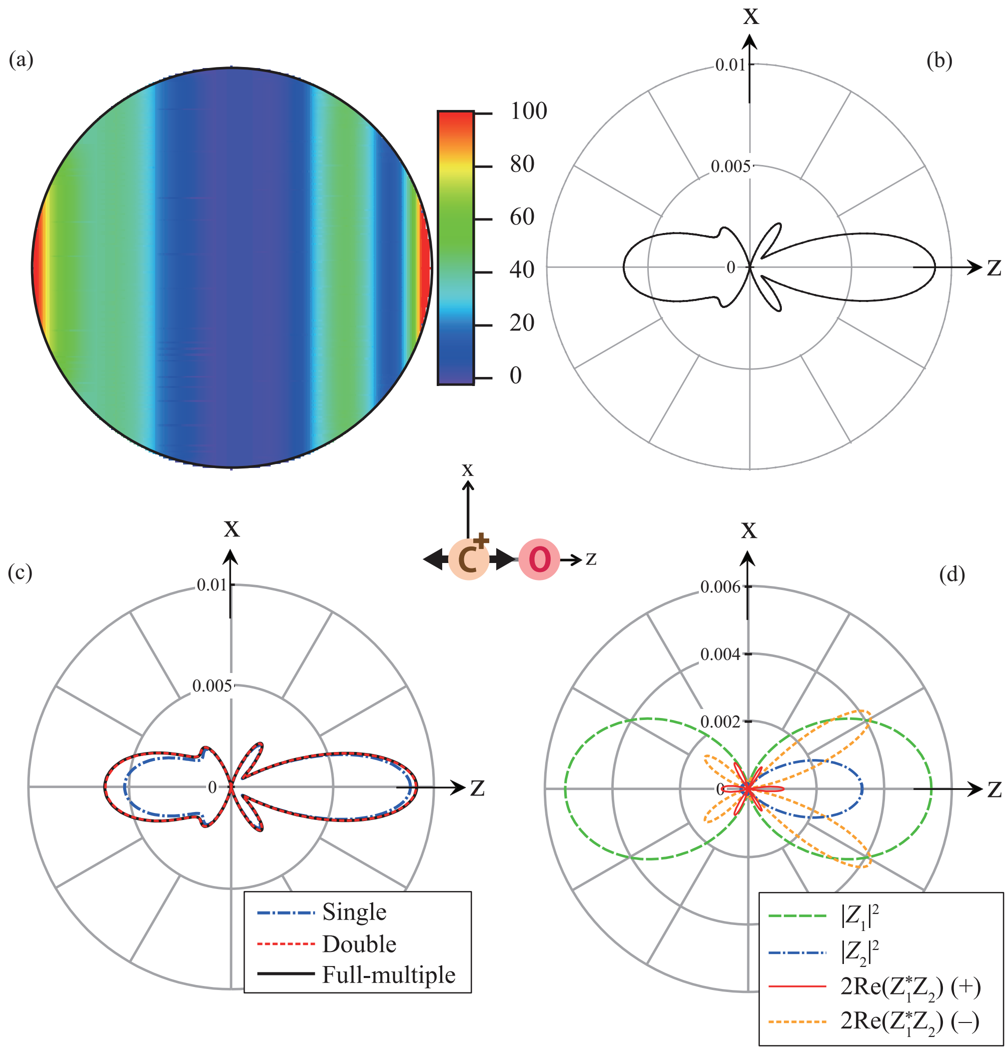

FIG. 2. (Color online) (a) Calculated two-dimensional C 1s XPD image of CO molecules at $\varepsilon_p = 150$ eV and (b) polar plot of the XPD. (c) Profiles of single ($|Z_1 + Z_2|^2$), double ($|Z_1 + Z_2 + Z_3|^2$), and full multiple scattering. (d) Components of the single-scattering intensity. In (c), the results for double scattering and full multiple scattering almost perfectly overlap. In (d), positive and negative values for $2\mathrm{Re}(Z_1^*Z_2)$ are shown separately.

2. *XPD pattern of $C_2H_4I_2$*

Here we discuss the diffraction patterns for rather complicated system, i.e., 1,2-diiodoethane $C_2H_4I_2$, the ground-state geometry of which is anti form. Transient structures of reaction intermediates of this molecule have been extensively studied by time-resolved electron and x-ray diffraction experiments so far [46,47]. We consider two conformations: one is the anti form, and the other is a structure with a dihedral angle of 0°, which is called the TS2 form in Ref. [48]. It is expected that the $C_2H_4I_2$ molecule takes the TS2 form in a transition state followed by photodissociation into the reaction intermediates [48]. Figure 3 shows calculated C 1s XPD patterns for the two conformations under the single-scattering approximation, which were constructed by the incoherent superposition of two XPD patterns for photoelectrons emitted from the left and right C atoms. The results for the anti form are shown in the left column and those for TS2 form are shown in the right column. The light polarization $\boldsymbol{e}$ is perpendicular to the C-C bond for both conformations, and the direction of $\boldsymbol{e}$ is defined as the z axis. The angular distributions of $|Z_1|^2$, $|Z_2|^2$, and $2\mathrm{Re}(Z_1^*Z_2)$ are shown together with the single-scattering XPD patterns. The photoelectron kinetic energy ε_p is changed from 100 to 500 eV. For both conformations, the profile of $|Z_2|^2$ shows strong forward scattering peaks toward iodine atoms. These peaks become sharper at higher kinetic energies because of the forward focusing effect. For all the XPD results, however, strong a destructive interference toward iodine atoms is observed and the forward scattering intensities are considerably canceled. The result for the anti form at $\varepsilon_p = 100$ eV shows strong peaks due to constructive interference around $\theta \sim 20^\circ$ and 200°, but this effect is hardly observed for higher kinetic energies. The profile of $|Z_2|^2$ for the TS2 form at $\varepsilon_p = 100$ eV shows small peaks due to backscattering by iodine atoms. As a consequence, a relatively strong interference effect is seen in the third and the fourth quadrants at that energy, and the profile of $|Z_1 + Z_2|^2$ shows

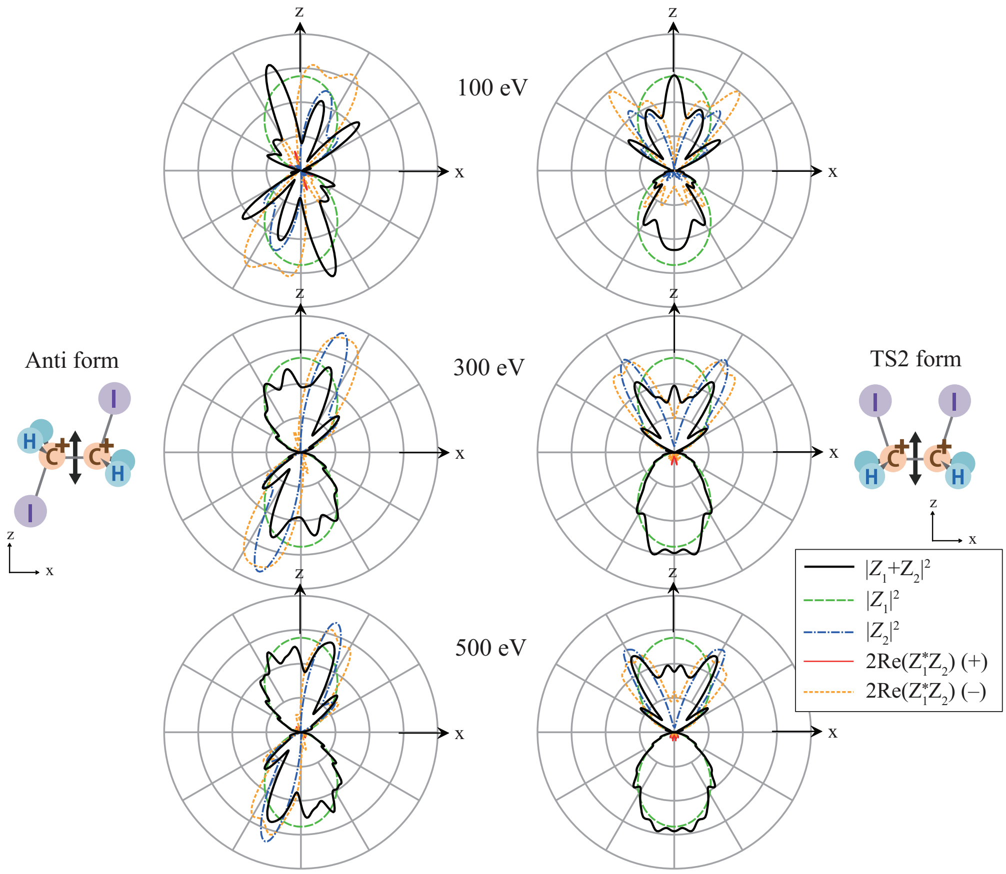

FIG. 3. (Color online) Polar plots of C 1s XPD for $C_2H_4I_2$. XPD patterns for the anti form are shown in the left column and those for TS2 form are given in the right column. Positive and negative values of $2\mathrm{Re}(Z_1^* Z_2)$ are shown separately. The positive value of the interference term is so small that it is hardly observed in the patterns. Insets: Molecular orientations and polarization vectors.

distinguishing structures in that direction. At higher kinetic energies, scattering effects are hardly observed in the lower half region because of the weak scattering power of hydrogen atoms. The profiles of $|Z_1 + Z_2|^2$ in that region show only small modulation from that of $|Z_1|^2$. These fine structures are easily blurred by finite acceptance angles of a detection system. Distinct or well-separated peaks of XPD patterns are preferable for determination of molecular structures by a "trial-and-error" method, which is discussed in Sec. III. Moreover, the number of distinct peaks of XPD patterns is linked to the accuracy of the structure parameters determined by this method. For these reasons, the kinetic energy range of 100–200 eV is thought to be the most preferable condition for structure determination of $C_2H_4I_2$. Calculated 2D C 1s XPD images and polar plots at $\varepsilon_p = 150$ eV are shown in Fig. 4. Full multiple scattering is taken into account there. A drastic change in the XPD patterns for the TS2 and anti forms is clearly shown. Both of the relevant polar plots show several distinct peaks and have a large potential to determine the molecular structure from XPD results.

III. METHODOLOGY OF MOLECULAR STRUCTURE DETERMINATION

We describe our new procedure to extract molecular geometric parameters from XPD patterns. It should be mentioned that we use our MFPAD data, which were obtained by the photoelectron–fragment-ion coincidence technique [49], as the XPD data.

Inner-shell XPD patterns contain rich information on molecular structure as discussed in Sec. II. To extract the information on the geometric parameters from the XPD patterns, we iterate a "trial-and-error" procedure comparing a set of experimental XPD patterns with the results of multiple-scattering XPD calculations with the use of trial model structures. Namely, trial XPD calculations are performed with varying molecular geometries such as bond length and bond angle, that is, by changing the position vector $\boldsymbol{R}_{\alpha A}$ and the Green's function $G_{L'L}(p\boldsymbol{R}_{\alpha A})$ in Eq. (24).

The quality of the fit between the theory and the experiment is evaluated by a reliability or R factor, which is a normalized square deviation summed over all data points of the XPD pattern for the emission directions of the photoelectrons [23, 50–52]:

$$R = \frac{\sum_\theta [I_{\mathrm{theor}}(\theta) - I_{\mathrm{exp}}(\theta)]^2}{\sum_\theta \left[I_{\mathrm{theor}}^2(\theta) + I_{\mathrm{exp}}^2(\theta)\right]}. \tag{27}$$

The intensities of I_{theor} and I_{exp} are normalized so that the area of each XPD pattern is unity. $R = 0$ corresponds to the perfect agreement and we seek the minimum value of the R factor, R_{min}. In the present trial-and-error procedure, calculated XPD patterns are convoluted over relevant experimental acceptance

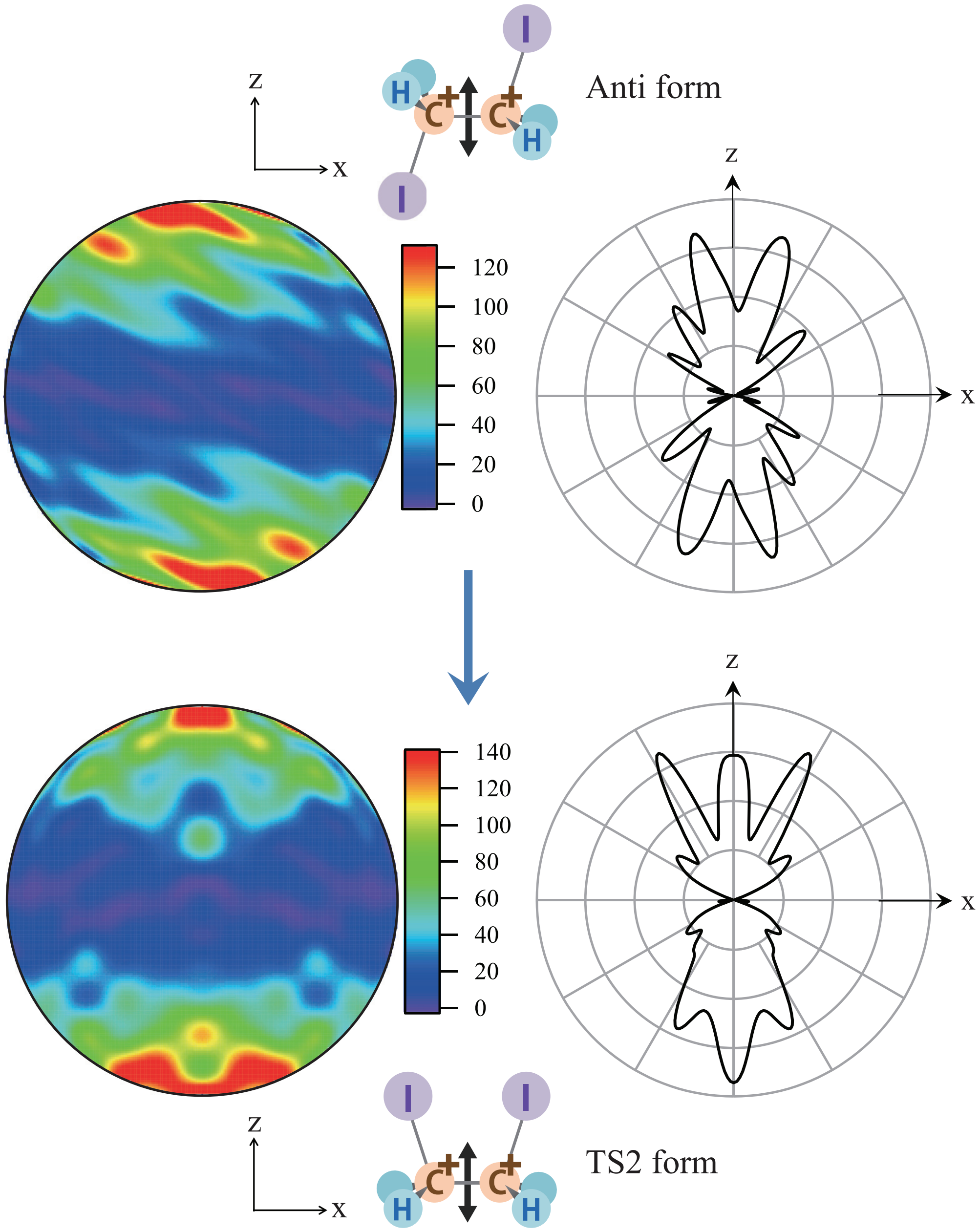

FIG. 4. (Color online) Calculated two-dimensional C 1s XPD images of $C_2H_4I_2$ molecule for the anti and TS2 forms at $\varepsilon_p = 150$ eV and polar plots of them. XPD patterns were calculated with full multiple scattering. Insets: Molecular orientations and polarization vectors.

angles of both photoelectrons and fragment ions. Proper regard for the acceptance angles is important to achieve a high accuracy of geometric parameters determined by the procedure. We have fitted experimental data by cosine functions, $\sum_{n=0}^{10} t_n \cos^n \theta$ (see Ref. [53]), and then used them as I_{exp}. Associated errors are estimated by the variance of R in the analogy of LEED analyses proposed by Pendry [50],

$$\text{Var}(R_{\text{min}}) = R_{\text{min}}\sqrt{(2/N_p)}, \tag{28}$$

where N_p is defined as the number of well-resolved peaks. All the parameter values giving structures with associated R factors $\leqslant R_{\text{min}} + \text{Var}(R_{\text{min}})$ are regarded as falling within one standard deviation of the best-fit structure. It is noted that the uncertainties evaluated by Eq. (28) are lower limits, because statistical errors of the experimental data are not included in the present procedure.

IV. APPLICATION OF MOLECULAR STRUCTURE DETERMINATION

In the application of the molecular structure determination procedure to our MFPAD data, we assume the following points *a priori*: (i) An inner-shell photoelectron will have left the vicinity of the molecule within a fraction of a femtosecond, and as a consequence, the relevant geometry is not the relaxed geometry but the initial-state geometry, so that (ii) the molecular structure obtained from the $R_{\rm min}$ is evaluated, referring to the equilibrium geometry in the ground state of the relevant molecules.

A. CO_2

The phase shift calculations were performed for an equilibrium C-O distance of 1.162 Å [54]. In the present "trial-and-error" method, we adopt this representative phase shift value for all the calculations of XPD for CO_2, assuming that a small difference in the phase shift due to a small change in the internuclear distance affects XPD patterns negligibly. Then the carbon 1s XPD patterns for the molecular z axis parallel to the light polarization have been calculated by changing the two bond lengths from 1.0 to 1.3 Å simultaneously. Figure 5(a) shows the calculated R factor as a function of the bond length, r(C-O). As shown, the R factor takes a minimum when $r(\text{C-O}) = 1.18$ Å. The length giving the $R_{\rm min}$ is indicated by the solid vertical line in the figure, and the equilibrium distance of r(C-O) in the ground state is shown by the dashed vertical line. The length determined by the present method is only 1.5% longer than the ground-state one, which is quite satisfactory. To get an intuitive impression of the XPD of the triatomic molecule, the 2D XPD image on the x-z plane at $R_{\rm min}$ is depicted in Fig. 5(b). Figure 5(c) shows polar plots of the calculated 2D XPD patterns at $R_{\rm min}$ and the maximum R [at $r(\text{C-O}) = 1.02$ Å] together with the experimental ones, which demonstrate the quality of the present method. That is, the polar plot of the XPD pattern is sensitive enough to extract the molecular structure from it. The values of r(C-O) for the CO_2 molecule determined by different methods are summarized in Table I.

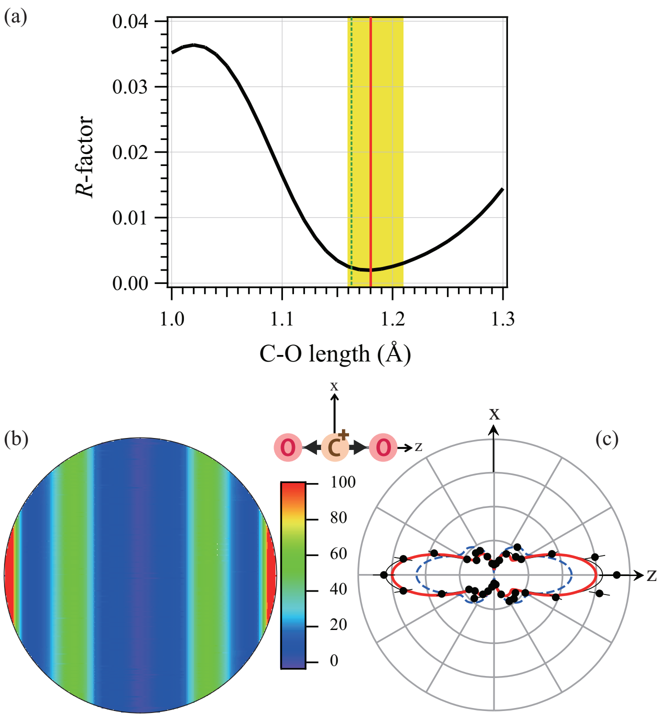

FIG. 5. (Color online) (a) R factor versus C-O bond length of CO_2: The solid vertical line indicates the C-O distance at the $R_{\rm min}$; the dashed vertical line, the equilibrium distance in the ground state; and the shaded (yellow) band, the range of the bond lengths with $R < R_{\rm min} + \text{Var}(R_{\rm min})$. (b) Calculated two-dimensional C 1s XPD image at the $R_{\rm min}$. (c) Polar plots of C 1s XPDs: Filled circles with error bars are the experimental data at $\varepsilon_p = 150$ eV; the thin solid curve, the fit of it, the bold solid curve, the XPD calculation at the $R_{\rm min}$; and the dashed curve, the calculation at the maximum R. The calculated results are integrated over the relevant experimental acceptance angles (in plane, ±10°; out of plane, ±20°; for both photoelectrons and fragment ions) to compare them with the experimental ones. Inset: Molecular orientation and polarization vector.

TABLE I. C-O bond length for a gas-phase CO_2 molecule. In the second column, the range of bond length with $R < R_{\rm min} + \text{Var}(R_{\rm min})$ is shown. The length with $R_{\rm min}$ is indicated in boldface.

	Present work	Equilibrium geometry [54]
r(C-O) (Å)	1.16–**1.18**–1.21	1.162

Further, we have checked the reliability of adopting a fixed value of the phase shift for the equilibrium geometry in spite of changing the bond length in the present trial-and-error method. For this, we have calculated the R factor using the values of the phase shift calculated for each trial model structure. Figure 6 shows the results. The R factor obtained by this procedure takes a minimum at the same r(C-O) as that for the fixed phase shift value. Moreover, the fitting accuracy at $R_{\rm min}$ is almost never improved. As a result, we can conclude that it is reasonable to adopt the fixed phase shift value obtained for equilibrium geometry throughout the R-factor evaluation.

B. NO_2

XPD data [55] for N 1s photoelectrons at $\varepsilon_p = 90$ eV for three polarization geometries have been examined by the present molecular structure determination method: perpendicular ($\boldsymbol{e} \parallel x$), perpendicular ($\boldsymbol{e} \parallel y$), and parallel ($\boldsymbol{e} \parallel z$) polarization with respect to the molecular z axis or C_2 axis. The nitrogen 1s XPD patterns have been calculated by changing both the two N-O bond lengths and the bond angle of O-N-O,

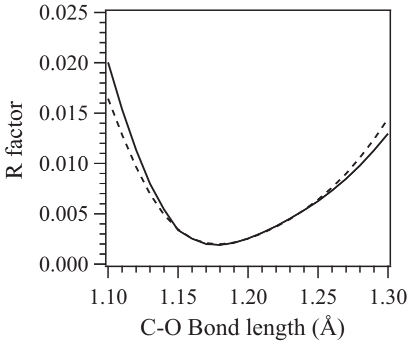

FIG. 6. Comparison between R factors calculated in two ways: The dashed line shows R calculated using the phase shift for the equilibrium geometry of CO_2 in the ground state, whereas the solid line indicates R calculated by phase shifts evaluated for each model structure.

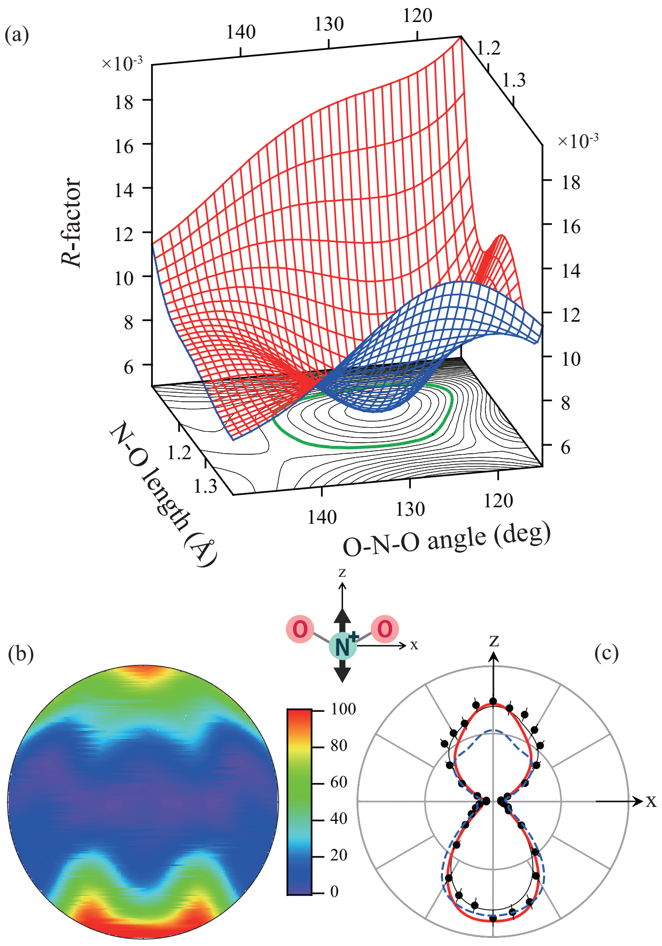

FIG. 7. (Color online) (a) R factor versus N-O bond length and O-N-O angle of NO_2. (b) Calculated two-dimensional N 1s XPD image at the $R_{\min}$. (c) Polar plots of N 1s XPDs: Filled circles with error bars are the experimental data at $\varepsilon_p = 90$ eV; the thin solid curve, the fit of it; the bold solid curve, the XPD calculation at the $R_{\min}$; and the dashed curve, the calculation at the maximum R. The calculated results are integrated over the relevant experimental acceptance angles for photoelectrons (in plane, $\pm 5^\circ$; out of plane, $\pm 30^\circ$) and fragment ions (in plane, $\pm 10^\circ$; out of plane, $\pm 20^\circ$) to compare them with the experimental ones. Inset: Molecular orientation and polarization vector. In (a), R takes values $< R_{\min} + \mathrm{Var}(R_{\min})$ inside the bold contour at the bottom.

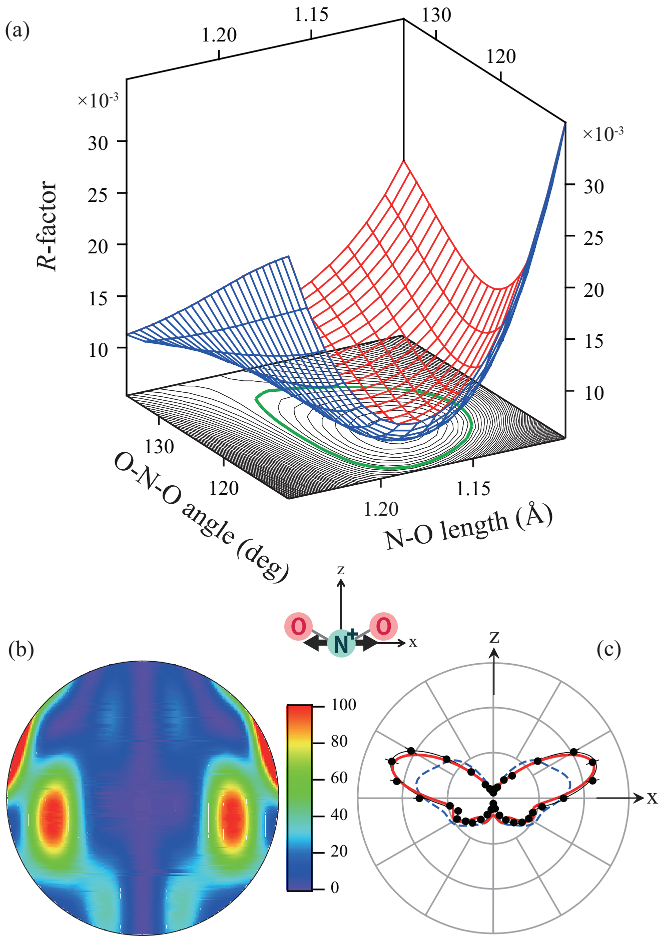

FIG. 8. (Color online) Same as Fig. 7 except for the perpendicular polarization geometry. Inset: Molecular orientation and polarization vector.

under the restriction that the NO_2 molecule maintains C_{2v} symmetry during the interaction with x rays.

The results obtained from the XPD data for a z axis parallel to the light polarization $\boldsymbol{e}$ are shown in Fig. 7. Figure 7(a) shows the calculated R factor as a function of the N-O length and O-N-O angle. A contour plot is shown at the bottom. The bold line in the contour plot indicates $R_{\min} + \mathrm{Var}(R_{\min})$. The R factor takes a minimum when $r(\text{N-O}) = 1.21$ Å and $\angle\text{ONO} = 128^\circ$. These structure parameters are compared with those of the equilibrium geometry in the ground state; 1.197 Å and 133.8° [54]. The differences between the molecular structure determined by the present method and the equilibrium geometry are $+1.1\%$ for the bond length and -4.3% for the bond angle. And the equilibrium geometry is in the region inside $R_{\min} + \mathrm{Var}(R_{\min})$. This verifies the validity of the present method. Figure 7(b) shows the calculated 2D XPD image at $R_{\min}$. The polar plots of the experimental and the calculated N 1s XPD patterns for both the $R_{\min}$ and the maximum R are given in Fig. 7(c). As shown in these figures, one can obtain more detailed information on the XPD for a bent molecule such as NO_2 in the 2D XPD image compared to the polar plot of the XPD, although, unfortunately, we cannot get a 2D image by our experimental technique at present. It should be noted that the 2D XPD data are more desirable than the polar plot data for molecular structure determination.

The results obtained from the XPD data for the perpendicular geometry ($\boldsymbol{e} \parallel x$) are given in Fig. 8. The R factor takes a minimum when $r(\text{N-O}) = 1.16$ Å and $\angle\text{ONO} = 118^\circ$. They differ by 3.2% for the bond length and 12% for the bond angle from those of the equilibrium geometry. The rather large disagreement on the bond angle might be due to the weak interference structure in the third and fourth quadrants of the XPD observed in the polar plot [see Fig. 8(c)]. In contrast to this, the 2D image exhibits a richly structured XPD as shown by increases or decreases in intensities [see Fig. 8(b)]. Thus, if one can use the 2D XPD data, one will be able to determine the molecular structure with less ambiguity. Furthermore, it should be mentioned that a photoelectron energy of $\varepsilon_p = 90$ eV is not the optimum condition to determine the molecular structure: In our computational experiment, the peaks shown at $\theta \sim \pm 70^\circ$

TABLE II. Geometric parameter values for a gas-phase NO_2 molecule. In the second column, the ranges of parameter values with $R < R_{\min} + \mathrm{Var}(R_{\min})$ are listed. Values with $R_{\min}$ are indicated in boldface.

	Present work	Equilibrium geometry [54]
r(N-O) (Å)		
($\boldsymbol{e} \parallel z$)	1.16–**1.21**–1.31	1.197
($\boldsymbol{e} \parallel x$)	1.13–**1.16**–1.20	
∠ONO (deg)		
($\boldsymbol{e} \parallel z$)	119–**128**–140	133.8
($\boldsymbol{e} \parallel x$)	111–**118**–132	

in Fig. 8(c) always appear for kinetic energies $\gtrsim$50 eV, although the peak positions move slightly depending on the energy. In the higher photoelectron energy region, additional peaks appear clearly in the third and the fourth quadrants which are barely observed at $\theta \sim \pm 125^\circ$ in Fig. 8(c): $\varepsilon_p = 90$ eV is the energy at which these peaks just start to appear. We confirmed by the computational experiment that these peaks in the third and fourth quadrants are formed by interference effects, i.e.; they contain rich information on the molecular structure. The geometric parameters determined by the present method are summarized together with those of the equilibrium geometry in Table II.

In the case of the out-of-plane geometry ($\boldsymbol{e} \parallel y$), the R factor does not take any minimum. This might be due to a weak scattering effect on the n y-z plane: The scatterer O atoms are out of the$y$-z plane, so that the geometry dependence of the XPD pattern must be weak. Thus we would like to say that the XPD data measured under this geometry are inadequate for structure determination.

C. BF_3

We used B 1s photoelectron angular distribution data [56] in the recoil frame of BF_2^+-F^+ as XPD data, because B 1s MFPAD data were not available. In these data, the orientations of the fragment ion BF_2^+ are averaged around the recoil axis. Then in the calculations, the relevant XPD patterns were obtained by averaging the XPDs for the oriented molecule over the azimuthal angle about the recoil direction. We have calculated the R factor by varying the bond length r(B-F) and the bond angle ∠FBF, under the restriction that three B-F bonds maintain the same length as each other and that the molecule changes from D_{3h} to C_{2v} symmetry. The result of the R factor is shown in Fig. 9. The R- factor takes a minimum when $r(\text{B-F}) = 1.15$ Å and $\vartheta = 139^\circ$ [see Fig. 9(a)]. Referring to the equilibrium geometry of $r(\text{B-F}) = 1.307$ Å and $\angle\text{FBF} = 120^\circ$, the length determined by the present method is 12% shorter and ϑ is 16% wider than those of the equilibrium values. These large differences imply that the recoil frame photoelectron angular distribution data do not give sufficient information for molecular structure determination with good accuracy. This is also shown by the large area of $R_{\min} + \mathrm{Var}(R_{\min})$ in the contour map at the bottom of Fig. 9(a). Figure 9(b) shows the richly structured 2D XPD image at the $R_{\min}$ for the molecular orientation shown in the figure. The polar plots of the calculated XPD patterns for both the $R_{\min}$ and the maximum R are shown together with the experimental data in Fig. 9(c). As shown in Figs. 9(b) and 9(c), one cannot obtain as much information on the molecular structure from the polar plot of the XPD for planar molecules such as BF_3. 2D XPD data may be necessary for molecular structure determination with a high accuracy. The geometric parameters determined by the present method are summarized together with those of the equilibrium geometry in Table III.

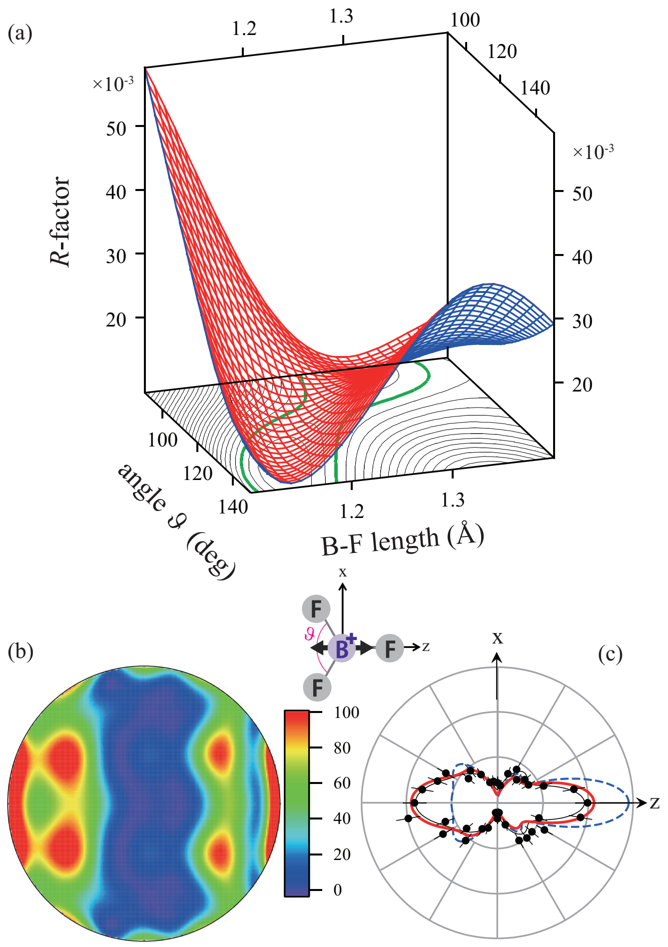

FIG. 9. (Color online) (a) R factor versus B-F bond length and angle ϑ of BF_3. (b) Two-dimensional B 1s XPD image at the $R_{\min}$. (c) Polar plots of B 1s XPDs: Filled circles with error bars are the experimental data at $\varepsilon_p = 120$ eV; the thin solid curve, the fit of it; the bold solid curve, the XPD calculation at the $R_{\min}$; and the dashed curve, the calculation at the maximum R. The calculated results are integrated over the relevant experimental acceptance angles for photoelectrons (in-plane, ±5°; out of plane, ±30°) and fragment ions (in plane, ±10°; out of plane, ±20°) to compare them with the experimental ones. Inset: Molecular orientation and polarization vector. In (a), R takes values $< R_{\min} + \mathrm{Var}(R_{\min})$ inside the bold contour at the bottom.

D. CH_3F

We used F 1s photoelectron angular distribution data in the recoil frame of CH_3^+-F^+ as XPD data, because F 1s MFPAD data were not available. In the calculations, the relevant XPD patterns were obtained by averaging the MFPADs over the

TABLE III. Geometric parameter values for a gas-phase BF_3 molecule. In the second column, the ranges of parameter values with $R < R_{\min} + \mathrm{Var}(R_{\min})$ are listed. Values with $R_{\min}$ are indicated in boldface.

	Present work	Equilibrium geometry [57]
r(B-F) (Å)	1.12–**1.15**–1.20	1.307
ϑ (deg)	110–**139**–	120

TABLE IV. Geometric parameter values for a gas-phase CH_3F molecule. In the second column, the ranges of parameter values with $R < R_{\min} + \mathrm{Var}(R_{\min})$ are listed. Values with $R_{\min}$ are indicated in boldface.

	Present work	Equilibrium geometry [58]
r(C-F) (Å)	1.31–**1.41**–1.47	1.383
∠HCF (deg)	110–**122**–	108.8

azimuthal angle about the recoil direction. The result of the R-factor evaluation is shown in Fig. 10. We have calculated R by varying the bond length r(C-F) and the bond angle ∠HCF under the following conditions: The bond length of C-H was fixed at that of the equilibrium geometry, 1.086 Å [58]. The three r(C-H) had the same length of 1.086 Å and the three ∠HCF kept the same value: The molecule held C_{3v} symmetry. The R factor takes a minimum when $r(\text{C-F}) = 1.41$ Å and $\angle\text{HCF} = 122^\circ$ [see Fig. 10(a)]. Referring to the equilibrium geometry of 1.383 Å and 108.8° [58], the r(C-F) determined by the present method is 2% longer and ∠HCF is 12% wider than that of the equilibrium values. One of the reasons for the large disagreement in the bond angle may be underestimation of the scattering power of hydrogen atoms. The muffin-tin radius for the hydrogen atom was estimated as 0.26 Å, which seems to be too small. It leads to an underestimation of the elastic scattering from hydrogen atoms. However, the quality of the results with the present method is better than that for BF_3; see the contour maps at the bottom of Figs. 9(a) and 10(a). This means that hydrogen atoms do not play as important a role in XPD. Figure 10(b) shows a 2D XPD image at the $R_{\min}$ for the molecular orientation shown. Polar plots of the experimental and calculated XPD patterns for both the $R_{\min}$ and the maximum R are shown in Fig. 10(c). As shown in Figs. 10(b) and 10(c), one can assume that detailed information on the molecular structure is not obtainable even from the 2D XPD image for prolate asymmetric top molecules such as CH_3F. 3D XPD data may be required for molecular structure determination with a higher accuracy. The geometric parameters determined by the present method are summarized together with those of the equilibrium geometry in Table IV.

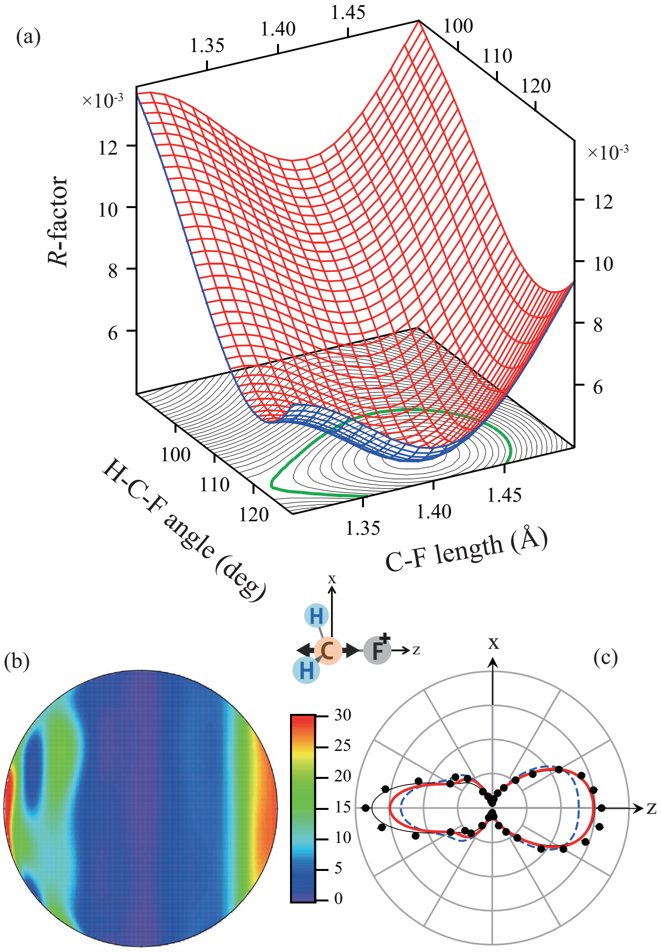

FIG. 10. (Color online) (a) R factor versus C-F bond length and H-C-F angle of CH_3F. (b) Two-dimensional F 1s XPD image at the $R_{\min}$. (c) Polar plots of F 1s XPDs: Filled circles with error bars are the experimental data at $\varepsilon_p = 150$ eV; the thin solid curve, the fit of it; the bold solid curve, the XPD calculation at the $R_{\min}$; and the dashed line, the calculation at the maximum R. The calculated results are integrated over the relevant experimental acceptance angles for photoelectrons (in plane, ±5°; out of plane, ±30°) and fragment ions (in plane, ±10°; out of plane, ±20°) to compare them with the experimental ones. Inset: Molecular orientation and polarization vector. In (a), R takes values $< R_{\min} + \mathrm{Var}(R_{\min})$ inside the bold contour at the bottom.

V. POSSIBLE EXPERIMENTAL SETUP

The XPD pattern of photoelectrons having energies from 100 to 200 eV is preferable for our molecular structure determination method as mentioned in Sec. II C2. Therefore we have designed a velocity map imaging spectrometer (VMIS) that satisfies the velocity focusing condition for photoelectrons with energies up to 200 eV. A schematic diagram of our photoelectron diffractometer consisting of two VMISs equipped with area detectors and supersonic pulsed molecular beams is shown in Fig. 11. To reduce the rotational temperature of the sample molecular gas, the molecular beam is formed by expanding a mixture of the carrier gas (typically 50 bar of helium) and the molecular gas (∼10 mbar) into the source chamber through a high-pressure Even-Lavie pulse valve [59,60]. The expanding molecular beam is collimated by a skimmer of 3-mm diameter (Beam Dynamics Model 50.8) positioned 120 mm downstream from the nozzle of 0.15-mm diameter of the Even-Lavie pulse valve and ejected into the target chamber through the skimmer. Under this condition, the sample gas density of $n \sim 10^{10}$ cm^{-3}

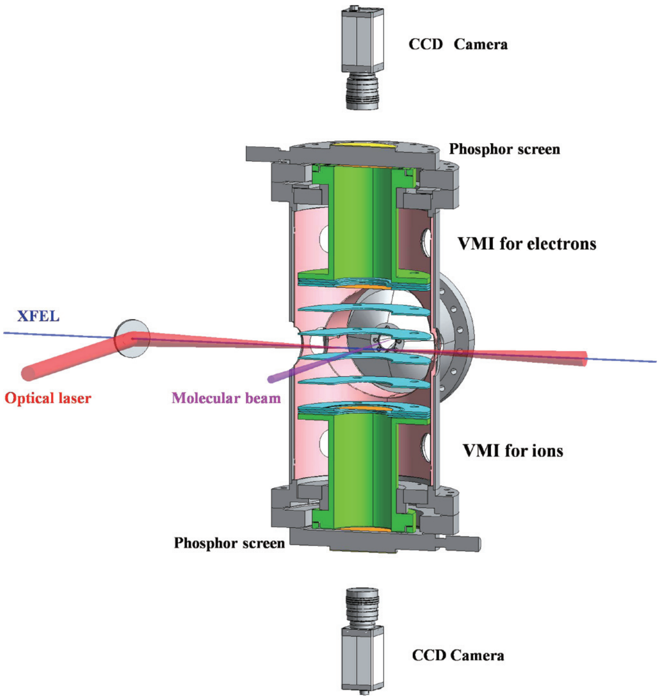

FIG. 11. (Color online) Schematic representation of the photoelectron diffractometer. Two beams propagating in a collinear arrangement intersect a molecular beam at the center of the diffractometer. An optical laser is used to align or orient the molecules that are probed by ionizing them using a time-delayed XFEL pulse. The XPD image is recorded by the upper VMI spectrometer. The degree of alignment or orientation is quantified using the 2D momentum distribution of the ionic fragments that is registered by the lower VMI spectrometer.

in the interaction zone at 150 mm downstream from the skimmer is estimated using the Monte Carlo simulation of G. Bird [61].

The target chamber houses the faced VMISs consisting of open disk electrodes, a drift tube, and 75-mm-diameter chevron microchannel plates backed by a similar-sized phosphor screen. Between the faced VMISs, the molecular beam is crossed by collinear pulsed laser beams (XFEL and optical laser) as indicated in Fig. 11. A uniform static electric field between the VMISs is produced by the potentials of the first front open disk electrodes with high-transmission mesh and compensation open disk electrodes between them. Then electrons are drawn into the upper VMIS, and ions into the lower VMIS. Electron images of the former and ion images of the latter are recorded by a charge-coupled-device (CCD) camera monitoring the fluorescent phosphor screen, and online software analysis determines and saves the coordinates of each individual particle hit. Trajectories of electrons with 200-eV energy calculated using SIMION [62] are shown in Fig. 12. As can be seen, electrons emitted from different source points in the interaction zone on the coplanar x-y plane including the propagation direction of XFEL and polarization of it make the outermost ring image due to the focusing action of the electrostatic lens, the radius of which is proportional to the velocity of the electrons. Electrons emitted out of the coplanar plane are detected inside the ring. Then we can measure the 2D image of the XPD pattern by the VMIS. It should be noted that in inner-shell photoionization, rather intense

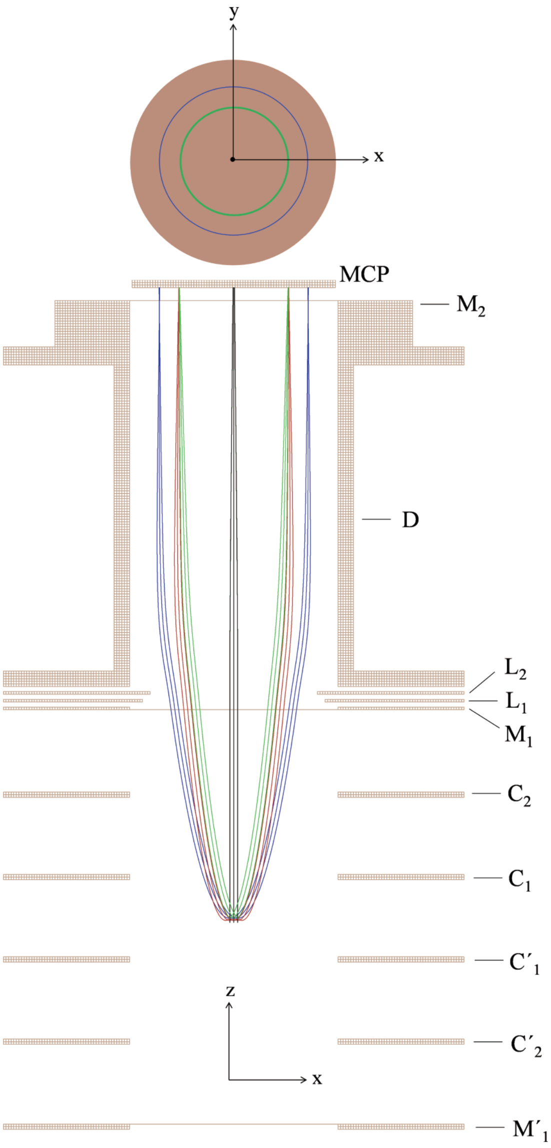

FIG. 12. (Color online) Detailed view of the VMIS for electron trajectory focusing. Two meshes, M_1 and M_2, delimit the extraction region (uniform extraction field) and the end of the drift tube of 80-mm diameter, respectively. The laser propagates along the x direction, causing a line source of 3-mm length, from which three external points, −1.5, 0, and 1.5 mm on the x axis, are chosen. From each point eight electrons with a 200-eV kinetic energy are ejected by the 45° angle spacing in the x-z plane. In the focusing plane on the MCP, electron trajectories of the same ejection angle but different positions come together. The trajectories focused at five points, from right to left, on the MCP correspond to ejection angles of 0° (+x direction), ±45°, ±90° (±z direction), ±135°, and 180° (−x direction), respectively. As the VMIS is cylindrically symmetric around the z axis, the electron trajectories are retained under the rotation of those around the z axis. This is indicated as circles in the upper figure. The potential condition of the electrodes for electron trajectory focusing is as follows: M_1 (M'_1), 10 kV (−10 kV); L_1, 10 kV; L_2, 10 kV; and D, 4.6 kV. The potentials of C_1 (C'_1) and C_2 (C'_2) are tuned to keep a uniform extraction field of 1.25 kV/cm: C_1 (C'_1), 1.9 kV (−1.9 kV); and C_2 (C'_2), 5.9 kV (−5.9 kV).

low-energy electrons are produced via shake processes. These low-energy electrons prevent us from using the full 2D data on the inner-shell XPD measured by the VMIS. To overcome this unwanted situation, tomographic imaging of photoelectrons, which constructs the 3D XPD from multiple projections, is promising [63]. The design of our diffractometer takes this situation into account: We can rotate the target chamber around the XFEL beam to measure the multiple projection images of the XPD.

The sample molecules in the molecular beam are controlled by the optical laser: Alignment of the molecules is achieved with intense nonresonant laser fields in the adiabatic regime (e.g., a Nd:YAG laser producing ∼10-ns pulses of 1024 nm and ∼500 mJ) or in the nonadiabatic regime (e.g., a Ti:sapphire laser providing ∼60-fs pulses of 800 nm and ∼400 μJ) [16]. The orientation of the molecules is formed by the combination of the YAG pulse and the static electric field between the VMISs [17–20] or an intense nonresonant two-color field in the adiabatic regime [21]. In addition, molecular alignment is realized by using a resonant excitation process of electronic states of the sample molecules, which is induced by ultrafast optical laser pulses in the ultraviolet region. In this case, taking the optical selection rule into account, one can control the alignment of the excited molecule at the instant of photoexcitation due to the polarization direction of the optical laser. This scheme is extremely interesting, because photochemical reactions, e.g., molecular deformation and elimination, are caused by such electronic transitions in the ultraviolet region. In this scenario, ultrafast molecular photoelectron diffraction images measured as a function of a delay time between the pump (optical laser)-probe (XFEL) pulses will be able to catch the molecular deformation or elimination driven by the optical laser.

The Spring-8 Angstrom Compact free-electron laser (SACLA) provides $N_{\text{ph}} \sim 10^{11}$ photons at up to 15 keV in 10-fs pulses at the maximum repetition rate of 60 Hz [64]. We estimate the photoelectron signal intensity based on these specification of the XFEL. Assuming that the electron detection efficiency of the 4π detection VMIS is unity, that the density n of the aligned or oriented molecular ensemble is $\sim 10^{10}$ cm^{-3}, and that the interaction length of the molecular beam and optical laser is ∼0.3 cm, we can estimate the number of recorded photoelectrons per pulse according to $N_e = 0.3 \times n\sigma N_{\text{ph}} \sim 10^2$. With a repetition rate of 60 Hz the corresponding rate will be $\sim 5 \times 10^3$ electrons per second. In this estimation, we used the photoionization cross-section data of $\sigma \sim 3 \times 10^{-19}$ cm^2 at 200 eV above the 1s ionization thresholds of the atoms in the second row in the periodic table [65]. This is because molecules consisting of such atoms are our targets. Moreover, the SACLA facility will provide soft x-ray FEL pulses with an energy of between 400 and 1000 eV in two years [66]. Such soft x-ray FEL is an ideal light source for our scenario, because the energy of it covers the 1s binding energies for elements ranging from carbon (288 eV) to neon (870 eV). To estimate the time required to record a snapshot of the XPD pattern, we refer to the XPD data shown in Sec. IV, which are the accumulation of $\sim 10^5$ triple-coincidence events between photoelectron and two fragment ions. From this, we can estimate for XFEL experiments that the accumulation of a few tens of seconds is sufficient to extract molecular structure information from the XPD data for small to medium-sized molecules at a certain delay between pump-probe pulses.

One of the most challenging aspects of the pump-probe experiment at SACLA is the spatial and temporal overlap between the optical laser and XFEL pulses. The overlap between the XFEL and the optical laser is made in a collinear arrangement (see Fig. 11). The coarse spatial overlap is done by monitoring the focal beam profile in the interaction region. A Ce:YAG screen is moved into the region, and then the phosphor fluoresces (scattered light) from the screen illuminated with the XFEL (optical laser) are monitored with a microscope. The coarse temporal overlap is done by monitoring the pulses from a photodetector (Hamamatsu Photonics, G4176-01 GaAs MSM) in the interaction region. The photodetector is moved into the region, and then pulses from the photodetector illuminated with the XFEL (optical laser) are monitored by a digital oscilloscope. It is noted that in order to prevent damage to the screen and photodetector, the XFEL as well as the optical laser should be substantially attenuated. Fine-tuning of the spatial and temporal overlap can be done using two-color signals; the 2D image of the mass-selected fragment ions, which is obtainable due to the electrical gate applied to the front of the MCPs, is monitored by the lower VMIS. The 2D image is also used to determine the degree of molecular alignment or orientation.

VI. SUMMARY

We have provided a molecular structure determination method, based on multiple-scattering XPD calculations. The new method has been applied to XPD data on several molecules having different equilibrium geometries, which were measured by the photoelectron–fragment-ion coincidence technique at the synchrotron radiation facility of the Photon Factory. As a result, it has been confirmed that geometric parameters, i.e., bond lengths with a resolution of <0.1 Å and bond angles with a resolution of <10°, can be determined by our method. The spatial resolution is sufficient to determine a transient molecular structure due to high-amplitude motions initiated by ultrashort optical lasers such as, for example, isomerization of azobenzene [67] and the roaming reaction of NO$_3$ radicals [68], although the spatial resolution <0.1 Å is inferior to that (typically <0.01 Å) obtained with electron diffraction. Such photochemical reactions proceed on a time scale of less than ∼1 ps, so that a time resolution of several tens of femtoseconds is demanded to observe a transient molecular structure across a transition state on the time scale of femtoseconds. When extended samples (e.g., 200 μm) are used like the molecular ensembles in the gas phase, pulsed electron diffraction encounters the so-called phase match problem: Due to the difference in velocity between the pump optical laser and the probe 30-keV electron pulse of about a factor of 4, the electron pulse needs picoseconds to travel the sample region. Such a phase mismatch appears not to be overcome by shortening the pulses, which is essentially absent in all optical setups. Using femtosecond pulsed photon beams from the XFEL, the molecular structure determination proceeds on an ultrafast time scale. That is, the large number of photoelectrons initiated by the ultrashort and high-intensity

XFEL pulses is extremely suitable for probing the time-dependent structure of the object molecule under investigation in pump-probe arrangements where the dynamics are induced either by an optical laser or by a replica of the XFEL pulse itself.

Differently from any other scenario of ultrafast structure determination until now, we measure the 2D or 3D XPD of aligned or oriented molecules in the energy range from 100 to 200 eV with a 4π detection VMIS. Our scenario exhibits the most probable method for obtaining ultrafast real-time structural information for small to medium-sized molecules consisting of light elements, in other words, a "molecular movie."

ACKNOWLEDGMENTS

We thank Dr. Tetsuya Ishikawa and Dr. Makina Yabashi for their useful comments on this project. The experiments were performed under the approval of the Photon Factory Program Advisory Committee (Projects No. 2009G560 and No. 2011G512). The present project was supported by a Grant-in-Aid for Scientific Research from the Japanese Ministry of Education, Culture, Sports, Science and Technology, MEXT (Grant No. 22244051), and by the Global COE program at Chiba University (Advanced School for Organic Electronics: G03, MEXT). M. Kazama is grateful for the financial support of a Grant-in-Aid for JSPS Fellows.

[1] M. Lein, J. Phys. B **40**, R135 (2007).
[2] S. Haessler, J. Caillat, and P. Salieres, J. Phys. B **44**, 20301 (2011).
[3] R. Neutze, R. Wouts, D. van der Spoel, E. Weckert, and J. Hajdu, Nature (London) **406**, 752 (2000).
[4] Z. Jurek, G. Faigel, and M. Tegze, Eur. Phys. J. D **29**, 217 (2004).
[5] S. P. Hau-Riege, R. A. London, and A. Szoke, Phys. Rev. E **69**, 051906 (2004).
[6] M. Bergh, N. O. Timneanu, and D. van der Spoel, Phys. Rev. E **70**, 051904 (2004).
[7] J. R. Fienup, Appl. Opt. **21**, 2758 (1982).
[8] D. Sayer, H. N. Chapman, and J. Miao, Acta Crystallogr. A **54**, 232 (1998).
[9] J. Miao, P. Charalambous, J. Kirz, and D. Sayre, Nature **400**, 342 (1999).
[10] S. Marchesini, H. He, H. N. Chapman, S. P. Hau-Riege, A. Noy, M. R. Howells, U. Weierstall, and J. C. H. Spence, Phys. Rev. B **68**, 140101 (2003).
[11] H. N. Chapman *et al.*, J. Opt. Soc. Am. A **23**, 1179 (2006).
[12] H. N. Chapman *et al.*, Nat. Phys. **2**, 839 (2006).
[13] M. M. Seibert *et al.*, Nature (London) **470**, 78 (2011).
[14] F. Krasniqi, B. Najjari, L. Struder, D. Rolles, A. Voitkiv, and J. Ullrich, Phys. Rev. A **81**, 033411 (2010).
[15] A. T. J. B. Eppink and D. H. Parker, Rev. Sci. Instrum. **68**, 3477 (1997).
[16] H. Stapelfeldt and T. Seideman, Rev. Mod. Phys. **75**, 543 (2003).
[17] H. Tanji, S. Minemoto, and H. Sakai, Phys. Rev. A **72**, 063401 (2005).
[18] H. Sakai, S. Minemoto, H. Nanjo, H. Tanji, and T. Suzuki, Phys. Rev. Lett. **90**, 083001 (2003).
[19] L. Holmegaard, J. H. Nielsen, I. Nevo, H. Stapelfeldt, F. Filsinger, J. Kupper, and G. Meijer, Phys. Rev. Lett. **102**, 023001 (2009).
[20] J. L. Hansen *et al.*, Phys. Rev. A **83**, 023406 (2011).
[21] K. Oda, M. Hita, S. Minemoto, and H. Sakai, Phys. Rev. Lett. **104**, 213901 (2010).
[22] C. S. Fadley, Surf. Sci. Rep. **19**, 231 (1993).
[23] D. P. Woodruff and A. M. Bradshaw, Rep. Prog. Phys. **57**, 1029 (1994).
[24] C. S. Fadley *et al.*, Prog. Surf. Sci. **54**, 341 (1997).
[25] C. S. Fadley *et al.*, J. Phys.: Condens. Matter **13**, 10517 (2001).
[26] D. P. Woodruff, Surf. Sci. Rep. **62**, 1 (2007).
[27] M. Kazama, J. Adachi, H. Shinotsuka, M. Yamazaki, Y. Ohori, A. Yagishita, and T. Fujikawa, Chem. Phys. **373**, 261 (2010).
[28] J. Adachi, M. Kazama, T. Teramoto, N. Miyauchi, T. Mizuno, M. Yamazaki, T. Fujikawa, and A. Yagishita, J. Phys. B. **45**, 194007 (2012).
[29] M. Kazama, H. Shinotsuka, T. Fujikawa, M. Stener, P. Decleva, J. Adachi, T. Mizuno, and A. Yagishita, J. Electron Spectrosc. Relat. Phenom. **185**, 535 (2012).
[30] E. Shigemasa, J. Adachi, M. Oura, and A. Yagishita, Phys. Rev. Lett. **74**, 359 (1995).
[31] A. Yagishita, K. Hosaka, and J. Adachi, J. Electron Spectrosc. Relat. Phenom. **142**, 295 (2005).
[32] K. L. Reid, Annu. Rev. Phys. Chem. **54**, 397 (2003).
[33] K. L. Reid, Mol. Phys. **110**, 131 (2012).
[34] J. Phys. B **45** (Special Issue) (2012).
[35] W. Bardyszewski and L. Hedin, Phys. Scripta **32**, 439 (1985).
[36] L. Hedin, J. Michiels, and J. Inglesfield, Phys. Rev. B **58**, 15565 (1998).
[37] C. Caroli, D. Lederer-Rozenblatt, B. Roulet, and D. Saint-James, Phys. Rev. B **8**, 4552 (1973).
[38] T. Fujikawa and H. Arai, J. Electron Spectrosc. Relat. Phenom. **123**, 19 (2002).
[39] C.-O. Almbladh and L. Hedin, in *Handbook on Synchrotron Radiation*, edited by E. E. Koch (North-Holland, Amsterdam, 1983), Vol. 1b.
[40] T. Fujikawa and L. Hedin, Phys. Rev. B **40**, 11507 (1989).
[41] T. Fujikawa, J. Phys. Soc. Jpn. **50**, 1321 (1981).
[42] H. Shinotsuka, H. Arai, and T. Fujikawa, Phys. Rev. B **77**, 085404 (2008).
[43] H. A. Bethe and E. E. Salpeter, *Quantum Mechanics of One- and Two-Electron Atoms* (Academic Press, New York, 1957).
[44] T. Fujikawa, R. Suzuki, H. Arai, H. Shinotsuka, and L. Kövér, J. Electron Spectrosc. Relat. Phenom. **159**, 14 (2007).
[45] T. Fujikawa, K. Hatada, and L. Hedin, Phys. Rev. B **62**, 5387 (2000).
[46] H. Ihee, V. A. Lobastov, U. M. Gomez, B. M. Goodson, R. Srinivasan, and A. H. Zewail, C.-Y. Ruan, Science **291**, 458 (2001).
[47] H. Ihee, M. Lorenc, T. K. Kim, Q. Y. Kong, M. Cammarata, J. H. Lee, S. Bratos, and M. Wulff, Science **309**, 1223 (2005).

[48] Q. Kong, J. Kim, M. Lorenc, T. K. Kim, H. Ihee, and M. Wulff, J. Phys. Chem. A **109**, 10451 (2005).

[49] K. Hosaka, J. Adachi, A. V. Golovin, M. Takahashi, N. Watanabe, and A. Yagishita, Jpn. J. Appl. Phys. **45**, 1841 (2006).

[50] J. B. Pendry, J. Phys. C **13**, 937 (1980).

[51] J. N. Andersen, H. B. Nielsen, L. Petersen, and D. L. Adams, J. Phys. C: Solid State Phys. **17**, 173 (1984).

[52] R. Terborg *et al.*, Surf. Sci. **466**, 301 (2000).

[53] V. V. Kuznetsov, N. A. Cherepkov, G. H. Fecher, and G. Schonhense, J. Chem. Phys. **117**, 7180 (2002).

[54] G. Herzberg, *Molecular Spectra and Molecular Structure: III. Electronic Spectra and Electronic Structure of Polyatomic Molecules* (Van Nostrand–Reinhold, New York, 1966).

[55] M. Yamazaki, J. Adachi, Y. Kimura, M. Stener, P. Decleva, and A. Yagishita, J. Chem. Phys. **133**, 164301 (2010).

[56] T. Mizuno, J. Adachi, M. Kazama, M. Stener, P. Decleva, and A. Yagishita, Phys. Rev. Lett. **110**, 043001 (2013).

[57] M. D. Harmony, V. W. Laurie, R. L. Kuczkowski, R. H. Schwendeman, D. A. Ramsay, F. J. Lovas, W. J. Lafferty, and A. G. Maki, J. Phys. Chem. Ref. Data **8**, 619 (1979).

[58] T. Egawa, S. Yamamoto, M. Nakata, and K. Kuchitsu, J. Mol. Struct. **156**, 213 (1987).

[59] U. Even, J. Jortner, D. Noy, N. Lavie, and C. Cossart-Magos, J. Chem. Phys. **112**, 8068 (2000).

[60] M. Hillenkamp, S. Keinan, and U. Even, J. Chem. Phys. **118**, 8699 (2003).

[61] http://www.gab.com.au/.

[62] D. A. Dahl, *SIMION 3D Version 7.0* (Idaho National Engineering and Environmental Laboratory, Idaho Falls, 2005).

[63] C. Smeenk, L. Arissian, A. Staudte, D. M. Villeneuve, and P. B. Corkum, J. Phys. B **42**, 185402 (2009).

[64] T. Ishikawa *et al.*, Nature Photon. **6**, 540 (2012).

[65] E. B. Saloman, J. H. Hubbel, and J. H. Scofield, At. Data Nucl. Data Tables **38**, 1 (1988).

[66] M. Yabashi and T. Ishikawa, *XFEL/SPring-8 Beamline Technical Design Report Version 2.0* (RIKEN Harima Institute, Wako, Japan, 2010).

[67] M. Böckmann, N. L. Doltsinsis, and D. Marx, J. Phys. Chem. **114**, 745 (2010).

[68] M. P. Grubb, M. L. Warter, H. Xiao, S. Maeda, K. Morokuma, and S. W. North, Science **335**, 1075 (2012).